

PLASTIC DAMPING OF ALFVÉN WAVES IN MAGNETAR FLARES
AND DELAYED AFTERGLOW EMISSION

XINYU LI AND ANDREI M. BELOBORODOV

Physics Department and Columbia Astrophysics Laboratory, Columbia University, 538 West 120th Street, New York, NY 10027

Draft version June 14, 2021

ABSTRACT

Magnetar flares generate Alfvén waves bouncing in the closed magnetosphere with energy up to $\sim 10^{46}$ erg. We show that on a 10-ms timescale the waves are transmitted into the star and form a compressed packet of high energy density. This packet strongly shears the stellar crust and initiates a plastic flow, heating the crust and melting it hundreds of meters below the surface. A fraction of the deposited plastic heat is eventually conducted to the stellar surface, contributing to the surface afterglow months to years after the flare. A large fraction of heat is lost to neutrino emission or conducted into the core of the neutron star.

Subject headings: dense matter — magnetic fields — stars: magnetars — stars: neutron — waves

1. INTRODUCTION

Magnetars are luminous slowly rotating neutron stars powered by the decay of ultrastrong magnetic fields $B = 10^{14} - 10^{16}$ G (see e.g. Woods & Thompson (2006); Mereghetti (2008) for reviews). They have hot surfaces, produce nonthermal magnetospheric radiation and strong bursts of hard X-rays. Occasionally, magnetars produce giant flares with energies of $10^{44} - 10^{46}$ ergs. To date three giant flares have been observed from three magnetars. The main peak of the giant flare lasts ~ 0.3 s and can reach huge luminosities $\mathcal{L} \sim 10^{47}$ erg s⁻¹. Less powerful flares with $\mathcal{L} < 10^{43}$ erg s⁻¹ (often called “bursts”) occur much more frequently.

The flares are associated with a sudden change in the magnetospheric configuration, which could be triggered by an instability inside or outside the neutron star (Thompson & Duncan 1996). This cataclysmic event involves strong deviations from the magnetostatic equilibrium, launching waves of large amplitudes. Part of the released magnetic energy is promptly dissipated and converted to radiation, and part is stored in the excited waves.

In particular, Alfvén waves are generated with a total energy up to $\sim 10^{46}$ erg. They are trapped on the closed magnetic field lines, as the group velocity of Alfvén waves is parallel to the magnetic field. The fate of their energy is poorly known. It was proposed that the Alfvén waves can be damped through nonlinear processes (Thompson & Blaes 1998), which become efficient at very large amplitudes of the waves (see Section 5.2).

In this paper, we propose another mechanism of the Alfvén wave dissipation, which results from the wave interaction with the star. The waves are ducted along the magnetic field lines with nearly speed of light and reach the stellar surface on a millisecond timescale. In Section 2 we examine the wave interaction with the star and find that a significant fraction of the wave energy is transmitted into the stellar crust. The reflected waves keep bouncing in the magnetosphere, however in a few tens of milliseconds most of their energy is drained and deposited into the crust, in the form of a compressed shear wave packet. In Section 3, we show that this packet

causes strong plastic heating of the crust. In Section 4 we investigate the fate of heat deposited by the plastic damping of Alfvén waves. In particular, we evaluate the heat flux conducted back to the surface and the resulting surface luminosity, which should emerge long after the flare. Our results are discussed in Section 5.

2. WAVE TRANSMISSION INTO THE CRUST

The crust is nearly incompressible and supports shear waves which can be excited by the Alfvén waves impinging from the magnetosphere. Excitation of two-fluid crustal modes can be neglected, and the recent claim that magnetospheric Alfvén waves transform into crustal Hall waves (Lyutikov 2015) is incorrect. Hall waves propagating parallel to the magnetic field \mathbf{B} with frequency ω in the crust of density ρ have refraction index $\mathcal{N} = ck/\omega = \omega_{pe}/\sqrt{\omega\omega_B} \approx 10^9 \rho_{11}^{1/2} \omega_5^{-1/2} B_{14}^{-1/2}$ (we use the standard notation $X_m = X/10^m$ for a quantity X in cgs units). This implies a huge impedance mismatch with the magnetospheric Alfvén waves, which have $\mathcal{N} \approx 1$, and therefore their transformation to Hall waves is suppressed.¹ No significant separation between electron and ion velocities can occur on ms timescales, and the response of the crust to the external disturbance is essentially single-fluid.

2.1. Transmission coefficient

Consider a magnetospheric Alfvén wave of frequency ω impinging on the crust of the neutron star. For simplicity let us assume that the initial (unperturbed) magnetic field B_z is uniform and vertical, so the wave is propagating vertically along the z -axis, and the horizontal displacement $\xi(z)$ is along the y -axis. The plasma-filled magnetosphere and the crust are excellent conductors; therefore the magnetic field is frozen in the medium and the horizontal field B_y is related to the displacement by

¹ Only electrons move in a Hall wave (analogous to whistler in plasma physics) while ions are static. The velocity of the electron fluid $\mathbf{v}_H = \mathbf{j}/en_e$ is related to electric current $\mathbf{j} = (c/4\pi)\nabla \times \mathbf{B}$, which gives a tiny v_H because of the high electron density n_e in the crust. Therefore, the “two-fluid” (electron-ion) description is useful only for slow phenomena in the crust.

$B_y/B_z = \partial\xi/\partial z$. The wave speed in the magnetosphere is close to the speed of light c , and the wavelength is $\lambda_0 = 2\pi c/\omega$.

The wave propagation is described by the equation,

$$\left[\rho(z) + \frac{B_z^2}{4\pi c^2} \right] \frac{\partial^2 \xi}{\partial t^2} = \frac{B_z^2}{4\pi} \frac{\partial^2 \xi}{\partial z^2} - \frac{\partial \sigma}{\partial z}. \quad (1)$$

Here $\rho(z)$ is the mass density and $\rho + B_z^2/4\pi c^2$ can be thought of as the effective inertial mass density of the magnetized medium.² The first term on the right-hand-side describes the restoring force of magnetic tension, and the last term describes the force due to the shear stress in the medium.

In particular, if the medium is elastic with a shear modulus μ then $\sigma = -\mu s$, where $s = \partial\xi/\partial z$ is the strain of the elastic deformation. In this case, Equation (1) becomes a simple wave equation with the wave speed given by

$$v^2(z) = \frac{B_z^2/4\pi + \mu(z)}{B_z^2/4\pi c^2 + \rho(z)}. \quad (2)$$

In the magnetosphere, we will neglect the mass density ρ and the shear modulus μ , which gives $v = c$. In the crust, we will use the profiles $\rho(z)$ and $\mu(z)$ shown in Figure 1. The density profile is obtained from the relativistic hydrostatic equation using SLy equation of state (Haensel & Potekhin 2004) for a neutron star with mass $M = 1.4M_\odot$.³ The radius of the star is $R = 11.7$ km, and its surface gravitational acceleration is $g = (GM/R^2)(1 - r_g/R)^{-1/2} = 1.7 \times 10^{14} \text{ cm s}^{-2}$ where $r_g = 2GM/c^2$. For the shear modulus μ we use the fitting formula given by Piro (2005) and Sotani et al. (2007) for low and high densities.

As the wave propagates into the deeper crust, its speed is reduced and its wavelength is compressed,

$$\lambda(z) = \lambda_0 \frac{v(z)}{c}, \quad \lambda_0 = \frac{2\pi c}{\omega}. \quad (3)$$

The reflection of the wave occurs in the region where the characteristic scale-height for the change of $v(z)$,

$$h(z) = \frac{v}{|dv/dz|}, \quad (4)$$

is smaller than the wavelength $\lambda(z)$. Figure 2 shows $\lambda(z)$, $h(z)$, and the depth z_1 where they are equal. The typical value of z_1 is around 200 meters below the surface; its exact value depends on B_z .

The transmitted wave below z_1 has $\lambda \ll h$ and can be described in the WKB approximation. Then the wave displacement takes the form (e.g. Fitzpatrick (2013)),

$$\xi(z) = \frac{\text{const}}{Z^{1/2}(z)} \cos \left[\omega \left(t - \int_0^z \frac{dz'}{v(z')} \right) \right], \quad (5)$$

² This expression is approximate as it neglects the contribution from the horizontal field component B_y . In the models presented below, $B_y > B_z$ when the wave propagates into the crust; however, this only occurs in the dense region where $B^2/4\pi \ll \rho c^2$ and the magnetic field inertia anyway may be neglected. In the region where $B^2/4\pi \gg \rho c^2$ the wave amplitude $s = B_y/B_z < 1$ and it is acceptable to approximate $B^2 \approx B_z^2$.

³ The ultrastrong magnetic field significantly changes pressure where the electron Fermi energy is below the Landau energy. This impacts the density profile $\rho(z)$ at shallow depths. However, at depths of interest in this paper (where $\rho \gg 10^8 \text{ g cm}^{-3}$) this effect is small and neglected.

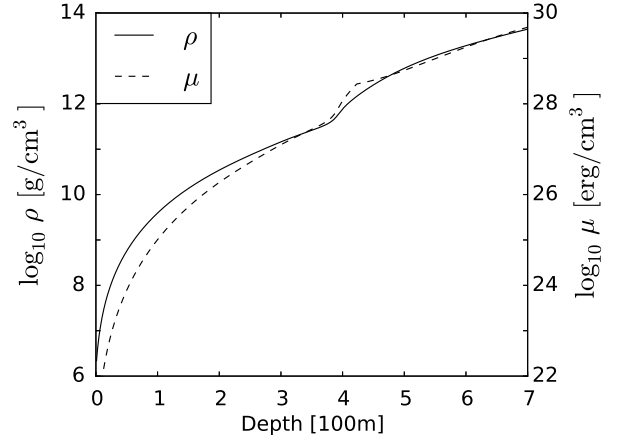


FIG. 1.— Density $\rho(z)$ and shear modulus $\mu(z)$ of the neutron star crust. The star is assumed to have mass $M = 1.4M_\odot$ and SLy equation of state.

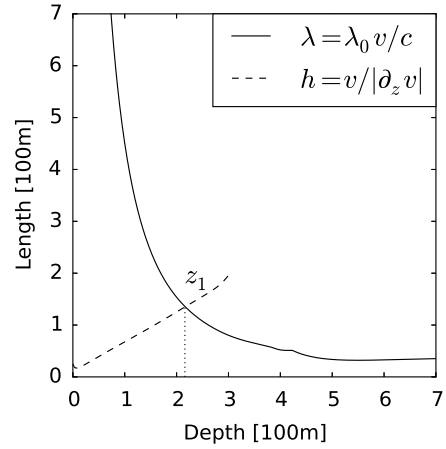


FIG. 2.— Solid curve shows the wavelength of the shear wave propagating in the magnetized crust, $\lambda = \lambda_0 v/c$, where $\lambda_0 = 10$ km and v is the speed of the wave. Dashed curve shows the characteristic scale-height of the wave deceleration, $h = v/|\partial_z v|$. A vertical magnetic field $B_z = 3 \times 10^{14} \text{ G}$ is assumed in this example.

where $Z(z)$ is the impedance,

$$Z(z) = \left[\frac{B_z^2}{4\pi} + \mu(z) \right]^{1/2} \left[\frac{B_z^2}{4\pi c^2} + \rho(z) \right]^{1/2}. \quad (6)$$

A simple estimate for the transmission coefficient is obtained using the impedance at z_1 (Blaes et al. 1989),

$$\mathcal{T} \sim \frac{4Z(z_1)Z(0)}{[Z(z_1) + Z(0)]^2} \approx \frac{4v(z_1)}{c}. \quad (7)$$

For instance, for $B_z = 3 \times 10^{14} \text{ G}$, Equation (7) gives $\mathcal{T} \sim 5\%$. A more accurate transmission coefficient is obtained by solving numerically the wave equation, which gives a higher value of $\mathcal{T} = 12\%$ (the smoothness of the crustal density variation as the wave approaches z_1 enhances the transmission). The numerically calculated $\mathcal{T}(B_z)$ is shown in Figure 3. It is comparable to 0.1 for typical magnetar fields.

The reflection coefficient $\mathcal{R} = 1 - \mathcal{T} \sim 0.9$ is large, and

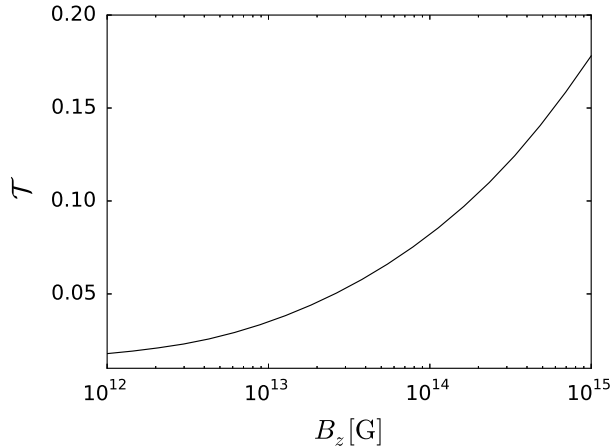


FIG. 3.— Transmission coefficient \mathcal{T} as a function of vertical magnetic field B_z , obtained from the numerical solutions of Equation (1).

the reflected Alfvén waves will bounce many times in the magnetosphere. Their amplitudes decrease by $\mathcal{T} \sim 10\%$ every time they bounce from the surface. The repeated transmission events form a train of compressed waves in the crust. This train propagates into the crust with velocity $v \sim 10^{-2}c$.

One can show from Equation (5) that the strain $s = \partial\xi/\partial z$ in the transmitted wave evolves as $|s| \propto v^{-1}Z^{-1/2} \propto \rho^{1/4}$. It *increases* as the wave propagates into the deeper and denser crust. This has a simple physical reason: the wave decelerates, and hence its energy density U_w grows as v^{-1} (so that the wave continues to carry its energy flux $F_w = U_w v = \text{const}$). The wave energy oscillates between the kinetic energy and the horizontal field plus elastic energy of the crust. Therefore, U_w may be written in two ways: $U_w \sim (\rho + B_z^2/4\pi c^2) \xi^2 \omega^2$ (kinetic) or $U_w \sim s^2 (B_z^2/4\pi + \mu)$ (magnetic+elastic). In the region where $\rho c^2 > B_z^2/4\pi$ and $\mu < B_z^2/4\pi$ this requires $\xi^2 \propto (\rho v)^{-1}$ and $s^2 \propto v^{-1}$. Then the relation $s \sim \xi/\lambda \propto \xi/v$ gives

$$\xi \propto v^{1/2}, \quad v \propto \rho^{-1/2}, \quad s \propto \rho^{1/4}. \quad (8)$$

In the lower crust where $\mu \gtrsim B_z^2/4\pi$ and $v \approx (\mu/\rho)^{1/2} \approx \text{const} \approx 10^8 \text{ cm s}^{-1}$ one finds $s \propto \rho^{-1/2}$. In this region the wave strain significantly decreases. This evolution of s with depth (increase and then decrease) may be observed in the numerical simulation presented below.

2.2. Numerical model

To illustrate the transmission process we set up a simple one-dimensional simulation of waves bouncing in the magnetosphere between the footprints of a closed magnetic flux tube. The Alfvén waves are ducted along the magnetic field lines and the problem can be made one-dimensional by pretending that the flux tube is straight, and by placing its two opposite footprints on the z -axis, separated by distance L . Here L represents the length of magnetospheric field lines. The stellar crust with the density profile $\rho(z)$ is placed symmetrically at the two ends of the computational box. The crust thickness $\sim 1 \text{ km}$ is much smaller than L .

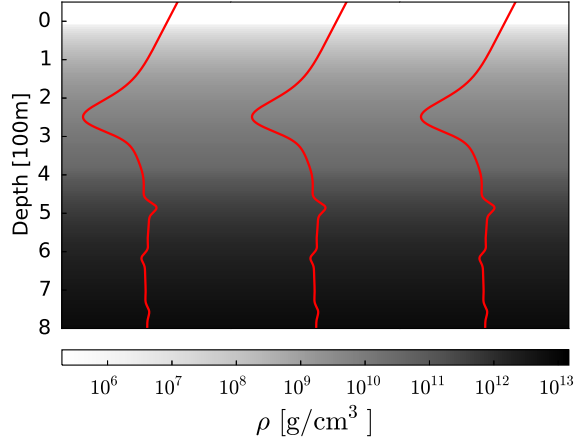


FIG. 4.— A snapshot of the wave after four reflection/transmission events. Solid red curves show the magnetic field lines deformed by the horizontal displacements in the wave; background grey color shows the density of the crust. The wave front has reached the depth of 800 m by this time. One can see the four oscillations in the transmitted and compressed packet. The shape of each oscillation reflects the initial shape of the magnetospheric wave assumed in the simulation. This simulation included no plastic dissipation and assumed the magnetic field $B_z = 3 \times 10^{14} \text{ G}$.

For any initial shear distortion of the field lines, one can calculate the subsequent dynamics of the generated Alfvén waves by solving numerically Equation (1). In our numerical models, we take the initial distortion of the form,

$$\xi_0(z) = A \exp \left[-\frac{(z - z_0)^2}{2l^2} \right], \quad (9)$$

which is localized in the middle of the box z_0 , far away from the crust, with $l < L$. The distortion immediately splits into two waves propagating toward the opposite ends of the box. The strain profile of each wave $s(z) = \partial\xi/\partial z$ is determined by the initial distortion. An important parameter of the wave is its initial maximum strain,

$$s_0 = \frac{1}{2} \max |\partial_z \xi_0(z)| = \frac{A}{2l} e^{-1/2}. \quad (10)$$

The total energy initially stored in the two waves is

$$E_0 = \frac{\sqrt{\pi}}{8\pi} B_z^2 \frac{A^2 S}{l}, \quad (11)$$

where S is the cross section area of the flux tube.

We follow the evolution of the waves and their interaction with the crust until almost all wave energy E_0 has been drained from the magnetosphere; this typically takes tens of light-crossing times L/c . The wave equation (1) is solved on a grid with 1000 points in the magnetosphere (uniformly spaced) and a much finer grid in the crust (one point per meter). Convergence tests have been done to ensure that the grid is sufficiently large to resolve the wave dynamics.

The snapshot of the simulation in Figure 4 shows the distortion of the crust at time $t = 4.6L/c$, when the magnetospheric waves have bounced four times. The parameters of this sample model are $L = 40 \text{ km}$, $l = 5/\sqrt{2} \text{ km}$, $A = 5 \text{ km}$, and $B_z = 3 \times 10^{14} \text{ G}$. The corresponding $s_0 = (2e)^{-1/2} \approx 0.43$ and $E_0/S \approx 4.5 \times 10^{32} \text{ erg cm}^{-2}$.

In the snapshot shown in the figure, about 1/3 of the wave energy E_0 has already been transmitted into the crust. The transmitted wave has been decelerated to $v \approx 10^8 \text{ cm s}^{-1}$ and compressed by the factor of $c/v \approx 3 \times 10^2$. The compression creates a high energy density of the horizontal magnetic field at $z = 200 - 500 \text{ m}$, $(sB_z)^2/8\pi \sim 10(s_0B_z)^2/8\pi$, and strain $s \sim 3s_0$.

3. PLASTIC HEATING

The description of the wave dynamics in Section 2 is incomplete because it assumes the elastic response $\sigma = -\mu s$ everywhere in the crust. The more realistic model must take into account two facts: (1) When the solid crust is deformed by the shear wave beyond a critical stress σ_{cr} its response becomes plastic rather than elastic. (2) The crustal temperature may be high enough to reduce σ_{cr} or even melt the crust, leading to $\sigma_{\text{cr}} \approx 0$. Therefore, the model should keep track of the crustal temperature.

3.1. Pre-flare temperature profile

The typical persistent surface temperature of magnetars is $T_s \sim (3 - 4) \times 10^6 \text{ K}$ (Woods & Thompson 2006). It corresponds to the radiation energy flux $F = \sigma T_s^4 \sim 10^{22} \text{ erg s}^{-1}$, where $\sigma = 5.67 \times 10^{-5} \text{ erg s}^{-1} \text{ cm}^{-2} \text{ K}^{-4}$ is the Stefan-Boltzmann constant. A usual way to estimate the subsurface temperature profile of neutron stars $T(z)$ assumes that the surface flux F is supplied by quasi-steady diffusion of heat from the crust. Then $T(z)$ is given by the equation,

$$\kappa(T, z) \frac{dT}{dz} = F = \sigma T_s^4, \quad (12)$$

where κ is the effective conductivity, which is dominated by degenerate electrons at densities $\rho > 10^6 \text{ g cm}^{-3}$ and by radiation in the low density layers near the surface. Note that κ depends on the local magnetic field. Combining Equation (12) with the hydrostatic equation $dP/dz = \rho g$ gives

$$\frac{d \log T}{d \log P} = \frac{3}{16} \frac{PK T_s^4}{g T^4}. \quad (13)$$

Here P is the pressure, $g = (GM/R^2)(1 - r_g/R)^{-1/2}$ is the surface gravitational acceleration, and $K = 16\sigma T^3/3\kappa\rho$ is the effective opacity; all quantities are measured in the local rest frame of the crust. The surface luminosity and temperature measured by a distant observer are $\mathcal{L}^\infty = (1 - r_g/R)\mathcal{L}$ and $T_s^\infty = (1 - r_g/R)^{1/2}T_s$ (Thorne 1977).

Equation (13) assumes that the temperature profile had enough time to relax to the steady state at depths of interest, which typically takes $\sim 1 \text{ yr}$. In a true steady state, the relatively high surface temperature of magnetars requires a source of heat at depths of a few hundred meters (Kaminker et al. 2006). Alternatively, one may view this temperature profile as quasi-steady, slowly cooling after a previous heating episode.

If one accepts this thermal model for the pre-flare state of the crust, one can find $T(z)$ from Equation (13) and determine the melting depth z_{melt} above which the crust is melted. We use the code of Potekhin (1999) to calculate the thermal conductivity and the melting point

$T_{\text{melt}}(\rho)$ of the crustal material. An approximate result is sufficient for the purposes of this paper and we do not discuss here the poorly known chemical composition of the magnetar crust. For simplicity, we assume an iron crust with a small impurity parameter.

We also assume that the pre-flare magnetic field is not far from vertical. This is a reasonable assumption for the melted layer ($z \lesssim 100 \text{ m}$, see below) where the crustal magnetic field should match the force-free magnetosphere. A strong toroidal field can only be stored in the core of the neutron star or the deep crust.

Equation (13) can be solved numerically as described in detail in previous works, which calculated the relation between the surface effective temperature T_s and the internal temperature T_b measured at neutron-drip depth $z_b \approx 400 \text{ m}$ ($\rho_b = 4 \times 10^{11} \text{ g cm}^{-3}$). In particular, Potekhin & Yakovlev (2001) provide a fitting formula for $T_b(T_s)$ for various magnetic fields and assuming an iron crust. We use this relation to impose the condition $T = T_b$ at $z = z_b$, and then reconstruct the profile $T(z)$ in the region of interest $\rho > 10^8 \text{ g cm}^{-3}$ (above or below z_b) by integrating Equation (13) from z_b . Thus we avoid integration in the shallow surface layers where thermal conductivity is dominated by radiation, and so we only use the electron conductivity in our calculations.

For a given T_s , this calculation gives the subsurface temperature profile $T(z)$ and the melting depth z_{melt} . The melting temperature is approximately given by

$$T_{\text{melt}} \approx 2.4 \times 10^9 \rho_{12}^{1/3} \text{ K}. \quad (14)$$

The exact value of melting depth z_{melt} depends on the magnetic field and its orientation relative to the stellar surface. A strong field increases the thermal conductivity along \mathbf{B} and decreases it perpendicular to \mathbf{B} . Therefore, a vertical field tends to reduce the internal temperature, thus decreasing z_{melt} . A horizontal field would hamper the heat flow in the vertical direction and increase z_{melt} . A typical z_{melt} in magnetars with non-horizontal surface fields is $\sim 100 \text{ m}$.

3.2. Plastic flow

As the wave packet propagates into the crust below z_{melt} , it starts to interact with the solid phase (lattice). The response of the lattice is elastic as long as its strain is below a critical value s_{cr} . The maximum $s_{\text{cr}} \sim 0.1$ is comparable to the yielding threshold for an ideal crystal (Chugunov & Horowitz 2010). The actual strain in the wave $s \sim s_0(\mathcal{T}c/v)^{1/2}$ is much higher than s_{cr} , and so the wave initiates a strong plastic flow with the high frequency ω . In contrast to fluid Alfvén wave or elastic shear wave, the plastic flow is dissipative, i.e. it converts the wave energy to heat, reducing its amplitude. Below we include this process in our wave propagation model.

The plastic heating rate per unit volume is

$$\frac{dU_{\text{th}}}{dt} = -\sigma \dot{s}_{\text{pl}}, \quad (15)$$

where $s_{\text{pl}} = s - s_{\text{el}}$ is the plastic part of the strain, s_{el} is the elastic part, and σ is the shear stress sustained by the plastic flow. In the plastic regime $|\sigma| > \sigma_{\text{cr}}$ where $\sigma_{\text{cr}} = \mu s_{\text{cr}}$. The simple model of “viscoplastic solid” (e.g. Irgens (2008)) gives the stress of the plastic flow in the

form,

$$|\sigma| = \sigma_{\text{cr}} + \eta|\dot{s}_{\text{pl}}|, \quad (16)$$

where η is a viscosity coefficient.

The crystal becomes “soft” (i.e. σ_{cr} drops) if it is heated to a temperature comparable to the melting point T_{melt} . The softening effect is responsible for the thermoplastic instability that can release internal magnetic stresses in magnetars (Beloborodov & Levin 2014). This instability however develops on a timescale much longer than 10 ms and does not affect the dynamics considered in this paper. Here the plastic flow is driven by the strong external magnetic stress from the flare (rather than develops spontaneously inside the crust) and immediately reaches huge strains $|s| \gg s_{\text{cr}}$ and high temperatures. Because $|s| \gg s_{\text{cr}}$, the detailed behavior of $s_{\text{cr}}(T)$ and $\sigma_{\text{cr}}(T)$ is not important; our calculation should merely take into account the fact that plastic heating switches off when T approaches T_{melt} .

This effect is included as follows: the stress σ of the plastic flow is multiplied by the factor $1 - U_{\text{th}}/U_{\text{melt}}$, where $U_{\text{th}}(\rho, T)$ is the thermal energy density and $U_{\text{melt}} = U_{\text{th}}(\rho, T_{\text{melt}})$. This prescription enforces $\sigma = 0$ when $T = T_{\text{melt}}$.

The stress in the elastic regime $\sigma = -\mu s$ must match the plastic stress at $s = s_{\text{cr}}$. This condition is automatically satisfied for the cold crystal. For a hot crystal the reduction of $\sigma_{\text{cr}}(T)$ may be interpreted as the reduction of shear modulus μ or the reduction of s_{cr} (or both). These details are not important for our model, because the plastic flow has $|s| \gg s_{\text{cr}}$. The numerical models presented below assume $s_{\text{cr}}(T) = 0.1 = \text{const}$ and use the following prescription for σ ,

$$\sigma = \left(1 - \frac{U_{\text{th}}}{U_{\text{melt}}}\right) \times \begin{cases} -\mu s, & \text{elastic} \\ (0.1\mu + \eta\dot{s}_{\text{pl}}) \text{sign}(-s), & \text{plastic} \\ 0, & \text{liquid} \end{cases} \quad (17)$$

where μ is the shear modulus at $T \ll T_{\text{melt}}$ shown in Figure 1, and one may think of $(1 - U_{\text{th}}/U_{\text{melt}})\mu$ as the shear modulus reduced by heating. We verified that practically the same results are obtained if we choose a temperature-dependent $s_{\text{cr}} = 0.1(1 - U_{\text{th}}/U_{\text{melt}})$ with shear modulus unchanged by heating.

Finally, we must choose η , which is unknown for the crustal material. The transition between the plastic and elastic regimes is smooth if η vanishes when $|s| = s_{\text{cr}}$. Therefore, we assume η of the form $\eta = \alpha\mu|s| - s_{\text{cr}}|$, where α is a constant. We tried various values of α and found that plastic heating weakly depends on it as long as α is sufficiently large, $\alpha > 3 \times 10^{-6}$ s. Our sample numerical models use $\alpha = 3 \times 10^{-5}$ s.

The dynamic system described by Equation (1) with σ given by Equation (17) satisfies the energy conservation law,

$$\frac{dQ}{dt} = S \int \frac{dU_{\text{th}}}{dt} dz = -\frac{d}{dt} (E_{\text{kin}} + E_B + E_{\text{el}}), \quad (18)$$

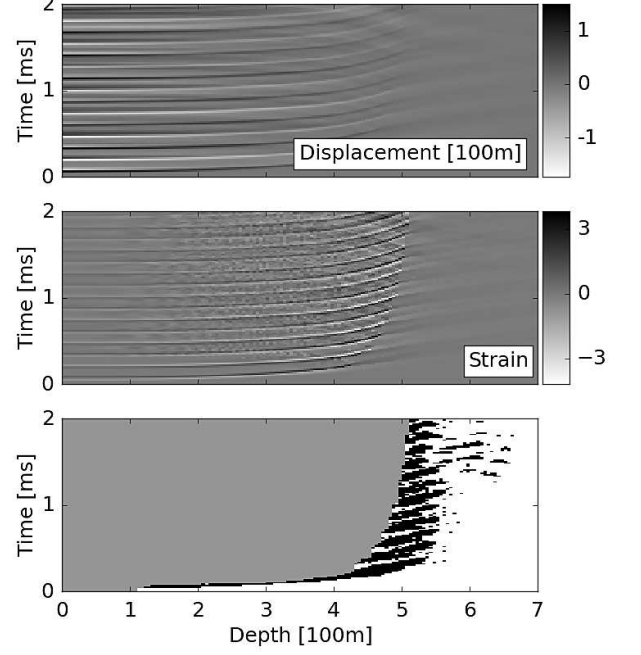


FIG. 5.— Shear wave propagation in the magnetar crust viewed on the spacetime diagram: Upper panel: horizontal displacement of the wave, ξ . Middle panel: strain $s = \partial\xi/\partial z$. Lower panel shows where the crust is deformed elastically (white), flowing plastically (black), and melted (gray).

where

$$E_{\text{kin}} = S \int \left(\rho + \frac{B_z^2}{4\pi c^2} \right) \frac{\dot{\xi}^2}{2} dz, \quad (19)$$

$$E_B = S \int \frac{s^2 B_z^2}{8\pi} dz, \quad (20)$$

$$E_{\text{el}} = S \int \frac{\mu s_{\text{el}}^2}{2} dz, \quad (21)$$

where $|s_{\text{el}}| < s_{\text{cr}}$ in the elastic zone and $|s_{\text{el}}| = s_{\text{cr}}$ in the plastic zone.

The plastic flow occurs where $|\sigma|$ exceeds σ_{cr} and continues as long as $d|s|/dt > 0$. Whenever the local absolute value of the strain stops growing, the plastic flow switches to the elastic regime; at this point s_{el} and σ are reset to zero.

3.3. Wave damping and post-flare crustal temperature

We re-run the model described in Section 2.2 with the new expression for σ that takes into account the plastic damping in the crust (Equation (17)). The initial state is assumed to have the surface temperature $T_s = 3 \times 10^6$ K. All other parameters are the same as in Section 2.2, in particular $B_z = 3 \times 10^{14}$ G and $s_0 = (2e)^{-1/2} \approx 0.43$. The spacetime diagram of the wave evolution in the crust is presented in Figure 5. It shows the wave displacement and strain, and indicates the elastic, plastic, and melted regions.

Figure 6 shows the history of the wave energy transmission from the magnetosphere to the crust and the plastic damping effect. One can see that most of the transmitted wave energy is promptly converted to heat. We have

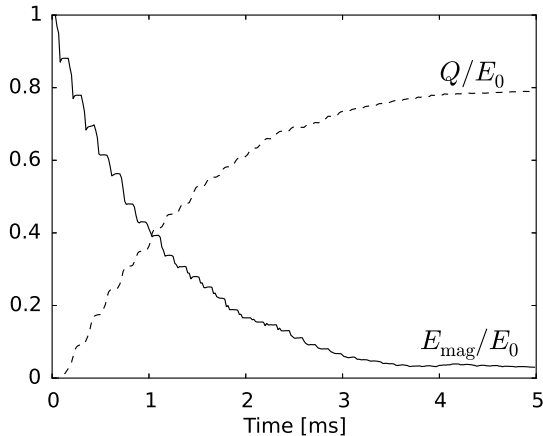


FIG. 6.— Solid curve shows the evolution of the energy fraction left in the magnetosphere and dashed curve shows the energy fraction converted to heat. Each step in the solid curve corresponds to the simultaneous reflection of the two symmetric waves bouncing in the magnetosphere in the opposite directions. The reflection coefficient $\mathcal{R} \approx 0.88$, and the magnetosphere loses energy as \mathcal{R}^N where N is the number of reflection events. Each step takes $L/c = (4/30)$ ms, so $E_{\text{mag}}/E_0 \approx 0.88^{t/0.133\text{ms}}$.

verified that our numerical simulation satisfies the conservation law (Equation (18)) with accuracy better than 1%. Each time the wave hits the surface, the transmission coefficient is approximately 12%, and almost all the wave energy E_0 is damped after ~ 10 ms, so most of E_0 becomes stored as crustal heat. This heating results in deep melting of the crust, down to 500 m.

Since plastic dissipation switches off at the melting point, the crust naturally acquires the “ceiling” temperature $T \approx T_m$ in an extended region below the surface. The resulting temperature profile immediately after the flare is shown in Figure 7. To investigate how the results depend on B_z and s_0 , we have calculated the models with $B_z/10^{14}$ G = 0.3, 1, 3, 10 and $s_0 = 0.13, 0.25, 0.43$. Stronger waves in stronger magnetic fields melt deeper layers of the crust, up to 600 m in the calculated models.

4. COOLING

After the flare, the hot crust will cool on a much longer timescale. Two main processes cool the crust: neutrino emission and heat conduction. The temperature evolution with time is described by the following equation,

$$C_V \frac{\partial T}{\partial t} = \frac{\partial}{\partial z} \left(\kappa \frac{\partial T}{\partial z} \right) - \dot{q}_\nu, \quad (22)$$

where κ is the thermal conductivity and C_V is the heat capacity of the crust; both are functions of local $\rho(z)$, $T(z, t)$, and \mathbf{B} . The sample numerical models presented below assume a uniform vertical magnetic field $B = B_z = \text{const}$. We use $\kappa(\rho, T, B)$ and $C_V(\rho, T, B)$ calculated by the code of Potekhin (1999). The term $\dot{q}_\nu(\rho, T, B)$ is the rate of local cooling by neutrino emission. This rate is described in detail by Potekhin & Yakovlev (2001). They provide useful analytical approximations for four relevant channels of neutrino emission: plasmon decay, bremsstrahlung, synchrotron, and electron-positron annihilation. We use their formulas in our calculations.

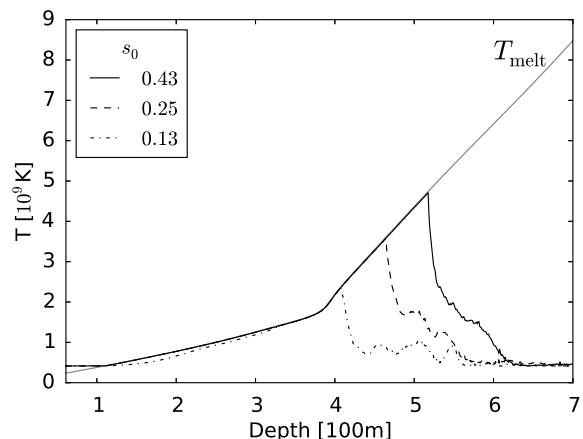
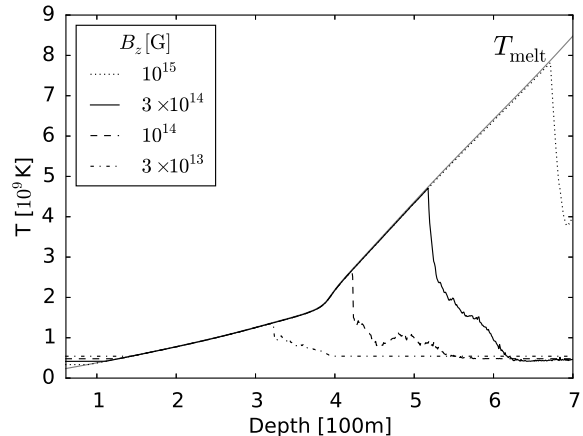


FIG. 7.— Temperature profile after the magnetospheric Alfvén waves have been absorbed by the crust; upper panel for fixed $s_0 = 0.43$ and different B_z , and lower panel for fixed $B_z = 3 \times 10^{14}$ G and different s_0 . The left boundary in the figure is chosen at depth $z \approx 60$ m where $\rho = 10^9$ g cm $^{-3}$; at $z \lesssim 100$ m the crust is melted before the flare, and hence no plastic heating can take place.

Similar to previous simulations of time-dependent heat diffusion in magnetars (Kaminker et al. 2006; Brown & Cumming 2009; Pons et al. 2009), we separate the crust into two regions: a blanketing envelope and an interior region. Here we choose the envelope boundary at $z_b \approx 60$ m where $\rho = \rho_b = 10^9$ g/cm 3 . The typical timescale of heat diffusion from this depth is $t_b \ll 10^6$ s. It is sufficiently short to give a quasi-steady state in the envelope, and so the steady-state solution may be used to determine the relation between $T_b = T(z_b)$ and the effective surface temperature T_s . Note that T_s defines the energy flux $F = \sigma T_s^4$ through the envelope $z < z_b$, and thus in essence the T_b - T_s relation is a relation between T_b and the heat flux $F = \kappa \partial T / \partial z$ at z_b . It serves as a boundary condition for our time-dependent heat diffusion problem at $z > z_b$. Since this boundary condition relies on the steady-state solution at $z < z_b$ it can only be accurate when $T(t, z > z_b)$ evolves on timescales longer than t_b .

We calculated the T_b - T_s relation at $\rho_b = 10^9$ g cm $^{-3}$ using the steady-state solutions obtained in Section 3.1. This gave a tabulated boundary condition $F(T_b)$ at the

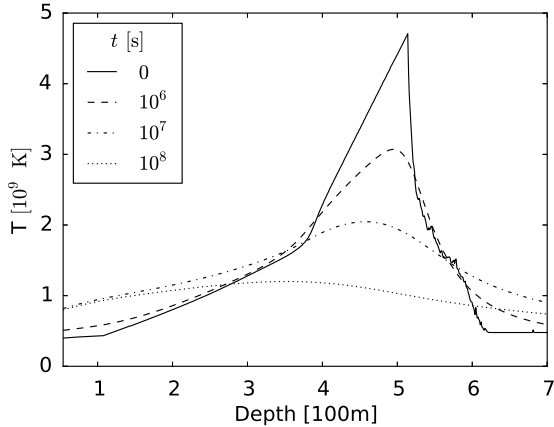


FIG. 8.— Evolution of the crustal temperature profiles in our fiducial flare model with $B = B_z = 3 \times 10^{14}$ G and $s_0 = 0.43$.

upper boundary of our computational box $z_b \approx 60$ m. The lower boundary is chosen at $z \approx 1$ km, near the bottom of the crust where $\rho \sim 10^{14}$ g cm $^{-3}$. The exact position of the lower boundary is not important as long as it is deep enough. The deep crust has a high thermal conductivity and the heat is absorbed by the (approximately isothermal) core of a huge heat capacity. We use the absorbing boundary condition at constant temperature $T \sim 3 \times 10^8$ K, neglecting the increase of the core temperature due to the absorbed heat.

The initial condition $T(z, 0)$ for Equation (22) is provided by the plastic heating model (Figure 7). The initial temperature increases along the melting curve $T_m(z)$, reaches maximum, and drops at larger depths. We evolve this initial temperature profile on a uniform grid of 1000 points and a time step of 10 s for 10^7 steps. To speed up the simulation, the values of κ , C_V , and \dot{q}_ν on the grid are updated every 500 time steps. Convergence tests verified that this resolution is sufficient to obtain accurate results. We also verified that our simulation conserves energy with better than 1% accuracy. The thermal energy lost by the crust is partially carried away by neutrinos and partially conducted through the boundaries.

Figure 8 shows the gradual evolution of the temperature profile $T(z)$ after the flare with the fiducial parameters (see Section 2.2 and Figures 5, 6). During the first month, the initial peak of temperature at $z \sim 500$ m is reduced from $\sim 5 \times 10^9$ K mainly due to neutrino losses. Then the peak continues to flatten and spread due to thermal conduction, forming a rather flat profile of $T \lesssim 10^9$ K in a few years.

We find that plasmon decay and bremsstrahlung make the dominant contributions to neutrino cooling, and synchrotron neutrino emission becomes significant in stronger magnetic fields $B_z \sim 10^{15}$ G. Electron-positron annihilation dominates neutrino cooling only in the shallow, low-density region of the crust, and its net contribution to the energy loss is negligible.

With increasing B_z (and at fixed amplitude s_0 of the waves excited in the flare) the deposited plastic heat increases, which increases the role of neutrino cooling. As a result, the relative contributions of plasmon decay, bremsstrahlung, and synchrotron neutrino emission depend on B_z . This dependence is shown in Figure 9, where

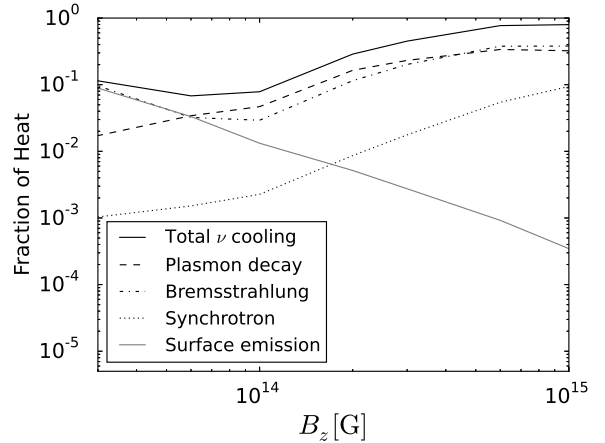


FIG. 9.— Fraction of the post-flare crustal heat lost through surface emission and various channels of neutrino emission, as a function of $B = B_z$. The flare is assumed to excite a pair of Alfvén waves with $s_0 = 0.43$ (Section 2.2) which are plastically damped in the crust.

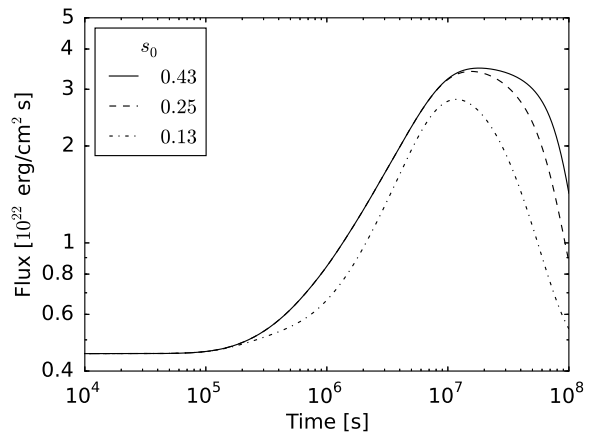
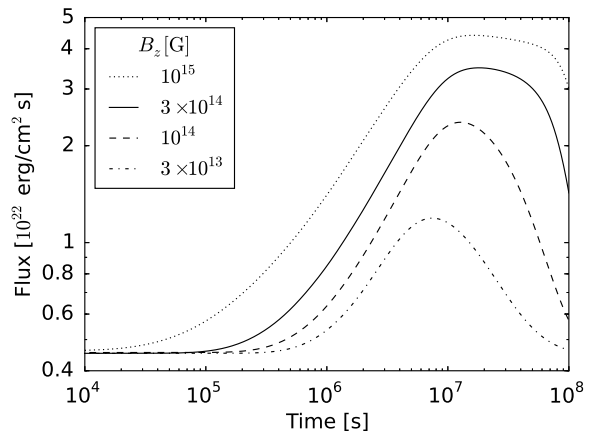


FIG. 10.— Surface thermal flux caused by the plastic heating in the giant flare. Upper panel: fixed $s_0 = 0.43$ and varying $B = B_z$. Lower panel: fixed $B_z = 3 \times 10^{14}$ G and varying s_0 .

we also show the energy fraction that is conducted to the stellar surface and radiated away. The remaining energy fraction (not shown in Figure 9) is conducted into the core of the neutron star.

One can see from Figure 9 that only a small fraction of the stored crustal heat is conducted to and radiated from the stellar surface. For example, at $B_z = 3 \times 10^{14}$ G less than 1% is conducted to the surface; roughly half of heat is lost neutrino emission and half is conducted to the core.

The heat radiated from the surface produces a delayed afterglow emission of the flare. The solution of Equation (22) gives the surface radiation flux F as a function of time. This flux is shown in Figure 10. One can see that the surface flux peaks with a significant delay after the flare — it takes the thermal conduction timescale (of months to years) to transport the crustal heat to the surface.

The core remains much colder than the plastically heated crust. The heat conducted to the core cannot significantly boost its temperature because (1) the core has a large heat capacity, so a huge energy $E_{\text{th}} \sim 10^{48} T_9^2$ erg would be required to heat it to e.g. 10^9 K (Yakovlev & Pethick 2004), and (2) the core is efficiently cooled by neutrino emission, and the cooling rate quickly grows at high temperatures.

5. DISCUSSION

5.1. Plastic damping and cooling

In this paper we described the phenomenon of plastic damping of Alfvén waves generated in magnetar flares. Our results may be summarized as follows.

(1) *Transmission.* The flare generates magnetospheric Alfvén waves with energy density

$$U_0 \sim \frac{\mu_B s_0^2}{2}, \quad (23)$$

where $\mu_B = B_z^2/4\pi$ is the tension of magnetic field lines, and $s_0 \gtrsim 0.1$ is the shear strain of the field lines. The waves are quickly transmitted into the crust of the neutron star. The transmission coefficient is $\mathcal{T} \sim 0.1$ (Figure 3), and most of the wave energy is transmitted after $N \sim \mathcal{T}^{-1} \sim 10$ reflection events (Figure 6). The transmitted waves form a train of N oscillations propagating with velocity $v \lesssim 10^{-2}c$ and compressed by the factor of c/v (Figure 4).

(2) *Compression.* The wave energy, which is initially spread in the magnetosphere, upon transmission becomes compressed. The energy density of the transmitted wave is

$$U_w \approx \mathcal{T} \frac{c}{v} U_0, \quad (24)$$

where v decreases to 10^8 cm s $^{-1}$ as the wave train propagates toward the bottom of the crust. The transmission occurs at depths z of a few hundred meters where the crustal density $\rho \sim 10^{10} - 10^{11}$ g cm $^{-3}$. In this region, U_w exceeds the maximum energy that could be stored in the elastic deformation of the crust, $U_{\text{el}} = \mu s_{\text{cr}}^2/2$, and the wave propagation is still sustained by the tension of

magnetic field lines, μ_B . Therefore, the transmission also leads to the strain amplification: $s^2/s_0^2 \approx U_w/U_0 \sim 10$.

(3) *Plastic flow.* The shear strain of the transmitted wave, $s \sim (\mathcal{T}c/v)^{1/2}s_0$, exceeds the maximum possible strain of elastic deformation $s_{\text{cr}} \sim 0.1$. Therefore, the wave induces a strong plastic flow of the crust, which dissipates the wave energy. A minimum plastic stress σ is comparable to μs_{cr} and may be higher, as the shearing motion is very fast and the viscoplastic term $\eta \dot{s}$ can dominate the stress. As the wave propagates into denser layers $\rho \sim 10^{12}$ g cm $^{-3}$, the shear modulus increases to $\mu \approx 10^{28} \rho_{12}$ erg cm $^{-3}$ (Figure 1). The plastic heat density deposited by the wave train is given by

$$U_{\text{th}} \sim \sigma s N \gtrsim \mu s_{\text{cr}} s N. \quad (25)$$

The high U_{th} given by this estimate implies that the wave energy density U_w converts to U_{th} , i.e. efficient damping occurs.

(4) *Melting.* Damping of the wave is buffered by melting — plastic damping is inefficient where the heated crust becomes nearly liquid, and the wave continues to propagate to denser layers that have a higher $T_{\text{melt}}(\rho)$. As a result, a simple temperature profile $T \approx T_{\text{melt}}(\rho)$ is created by the plastic flow in an extended region of the crust (Figure 7).

Most of the wave damping occurs at depth z_{damp} where T_{melt} is so high that the wave dissipation becomes marginally capable of melting the crust. Thus z_{damp} is also the depth of the melted region. At this depth the following condition is satisfied,

$$C_V T_{\text{melt}} \sim U_w. \quad (26)$$

We found $z_{\text{damp}} \sim 500$ m for a typical wave energy in magnetar giant flares and $B_z \sim 3 \times 10^{14}$ G (Figure 7). Deeper melting $z_{\text{damp}} \sim 700$ m is possible if the giant flare occurs in a flux rope of a particularly strong field $B_z \gtrsim 10^{15}$ G.

(5) *Cooling.* On a timescale of months to years, the deposited heat is mostly lost to neutrino emission and conducted into the core of the star (Figures 8 and 9). A modest energy E_{aft} is conducted to the stellar surface and emitted in a delayed afterglow radiation. A typical energy radiated per unit area is $E_{\text{aft}}/S \sim 10^{30}$ erg cm $^{-2}$. The timescale for the rise of afterglow luminosity is the thermal conduction time $t_{\text{cond}} \sim 10^7$ s. In a broad range of the flare parameters, the peak flux of surface afterglow is $F_{\text{max}} \sim (2 - 4) \times 10^{22}$ erg cm $^{-2}$ s $^{-1}$ (Figure 10).

There are ways to refine our model of surface afterglow from plastic damping of magnetospheric waves. All sample models shown in this paper assumed approximately vertical (radial) magnetic field in the upper crust. A strongly inclined field would significantly reduce thermal conductivity in the radial direction and delay the crustal cooling. It could also bolster a high crustal temperature before the flare, which would give a deeper melted zone where plastic damping would be impossible. In this case, the flare could only cause heating of the deep crust where practically all heat is wasted to neutrino emission and inward conduction. Thus, a strong non-radial field component tends to reduce the expected afterglow emission.

Our presented models assumed iron composition everywhere in the crust, including the blanketing envelope. Light element composition of the envelope would increase its thermal conductivity (Potekhin et al. 2003), decreasing the internal temperature and reducing the depth of the melted layer in the pre-flare crust. Therefore, if magnetars have a light element envelope, their post-flare cooling occurs faster. This effect somewhat increases the afterglow flux, especially at early times, and may offset the opposite effect of the non-radial magnetic field.

5.2. Other mechanisms of Alfvén wave damping

Nonlinear interactions of Alfvén waves in the magnetosphere provide an additional damping mechanism. The existing estimates (Thompson & Blaes 1998) suggest that this mechanism will be dominant at very high amplitudes of the waves, $s_0 \gtrsim 1$. The nonlinear interactions occur as the Alfvén waves bounce from the stellar surface and collide in the magnetosphere. The nonlinear terms in the electrodynamic equations show two types of wave interactions:

(1) $A + A \rightarrow F$: two Alfvén waves A convert into a fast magnetosonic wave F (which may escape the magnetosphere). The damping of Alfvén waves by this “3-wave” interaction occurs on the timescale,

$$t_{\text{damp}} \sim \frac{\lambda/c}{(k_{\perp}\xi)^2} \sim \left(\frac{k_{\parallel}}{k_{\perp}}\right)^2 \frac{\lambda/c}{s^2}, \quad (27)$$

where $\lambda = 2\pi/k_{\parallel}$ is the wavelength along \mathbf{B} (comparable to the length of the magnetospheric field line L), ξ is the characteristic displacement in the waves, and k_{\perp} is the wavevector component perpendicular to the magnetic field. The Alfvén waves, which are ducted along the curved magnetic field lines, may be expected to have $k_{\perp} \sim k_{\parallel}$.

(2) $A + A \rightarrow A + A$: two Alfvén waves generate two new Alfvén waves. This “4-wave” interaction initiates a cascade to high k_{\perp} , which may lead to the wave dissipation on small scales (Thompson & Blaes 1998). The damping time due to this higher-order process is

$$t_{\text{damp}} \sim \frac{\lambda/c}{(k_{\perp}\xi)^4} \sim \left(\frac{k_{\parallel}}{k_{\perp}}\right)^4 \frac{\lambda/c}{s^4}. \quad (28)$$

The time t_{damp} given by Equations (27) and (28) should be compared with $\mathcal{T}^{-1}L/c \sim 10L/c$, the lifetime of the Alfvén waves to transmission and plastic damping in the crust. The numerical coefficients in Equations (27) and (28) have not been calculated, however the estimates suggest that if the flare generates $s_0 \gtrsim 1$, the nonlinear wave interactions can reduce s_0 to a value $\lesssim 1$ before the waves are damped plastically in the crust.

The wave cannot be completely damped by the plastic mechanism. In particular, at strains $|s| < s_{\text{cr}}$ it propagates with no significant damping. The residual wave train will reach the bottom of the crust and enter the liquid core. It will travel through the core along the magnetic field lines and after time $\sim 2r/v$ (typically shorter than 1 s) the train will again emerge somewhere at the bottom of the crust and continue to propagate upward.

The low-amplitude waves will continue to travel through the magnetosphere and the star for a while. Their lifetime at any given amplitude s is limited by the

nonlinear interactions in the magnetosphere $t_{\text{damp}} \propto s^{-2}$. The Alfvén waves are also subject to gradual ohmic dissipation, as their propagation involves excitation of electric currents demanded by $\nabla \times \mathbf{B} \neq 0$. After the flare, the effective resistivity of the magnetosphere is controlled by the threshold voltage of electron-positron discharge that organizes to conduct the electric currents (Beloborodov & Thompson 2007).

5.3. Observed afterglow

Sudden crustal heating followed by gradual crustal cooling was proposed to power the afterglow of the giant flare in SGR 1900+14 (Lyubarsky et al. 2002). The afterglow was extremely bright in the first hours after the flare, $\mathcal{L} \sim 10^{37} - 10^{38} \text{ erg s}^{-1}$, and during the next month it showed a power law decay $\mathcal{L} \propto t^{-0.7}$ (Woods et al. 2001). Lyubarsky et al. (2002) explored how heat should be deposited to give the observed afterglow light curve and found that heating should be approximately uniform throughout the 500-m-deep layer below the surface. This implies, in particular, enormous heating in the shallow layers $z \ll 100 \text{ m}$. The heating mechanism in the low density layers is unclear and certainly cannot be provided by plastic dissipation. Therefore we do not attempt to explain the early afterglow of SGR 1900+14 by crustal heating. We also note that the afterglow spectrum was nonthermal (Woods et al. 2001), which suggests a magnetospheric source.

Plastic damping of magnetospheric Alfvén waves produces a well defined temperature profile of the crust: $T \approx T_{\text{melt}}(z)$ down to z_{damp} . This leads to specific predictions for the afterglow light curves (Figure 10), with the surface flux $F \sim (2 - 4) \times 10^{22} \text{ erg cm}^{-2} \text{ s}^{-1}$ on a timescale $\gtrsim 100 \text{ d}$. This flux and timescale appear to be consistent with observations of some less energetic “transient” magnetars after their bursting activity.

In particular, the luminosity of SGR 1627-41 after its outbursts in 1998 and 2008 showed a decay on a year timescale (Mereghetti et al. 2006; Esposito et al. 2008; An et al. 2012). The luminosity at $t \sim 100 \text{ d}$ was $\mathcal{L} \sim 7 \times 10^{34} (d/11 \text{ kpc})^2 \text{ erg s}^{-1}$ after the 1998 outburst and $\mathcal{L} \sim 2 \times 10^{34} (d/11 \text{ kpc})^2 \text{ erg s}^{-1}$ after the 2008 outburst, where the distance $d \approx 11 \text{ kpc}$ was inferred from the apparent location of SGR 1627-41 in a star-forming region (Hurley et al. 1999). The decay on a year timescale is consistent with the crust melting down to $z_{\text{damp}} \sim 300 \text{ m}$, and the observed luminosity \mathcal{L} is consistent with the melted crust area occupying $\sim 10\%$ of the stellar surface.

Swift J1822.3-1606 provides another example. It produced afterglow emission following the outburst in 2011 (Rea et al. 2012; Scholz et al. 2012, 2014). Similar to the afterglow of SGR 1627-41, its light curve may be described as a double exponential, with the second (longer) exponential component visible after $\sim 100 \text{ d}$. Scholz et al. (2014) used a crustal cooling model to describe both the early and late afterglow components in Swift J1822.3-1606. In their model, heat deposition is a phenomenological parameter adjusted to reproduced observations. We find that plastic damping of magnetospheric waves is only capable of explaining the late afterglow component, and the early component must invoke a different heat source. The late component has the

luminosity and decay timescale similar to those observed in SGR 1627-41, consistent with the crust melting down to $z_{\text{damp}} \sim 300$ m.

A reliable identification of the crustal afterglow is complicated by the presence of another, *nonthermal*, emission component. The nonthermal source is likely present during the afterglow of SGR 1627-41 (An et al. 2012), and nonthermal hard X-rays are unambiguously detected in the transient magnetar 1E 1547.0-5408 during its afterglow following the 2009 outburst (Enoto et al. 2012; Kuiper et al. 2012). The nonthermal activity is usually associated with the twisted equilibrium magnetosphere, which carries persistent electric currents (Thompson et al. 2002; Beloborodov 2013). The twist is ohmically dissipated over a year timescale, which happens to be comparable to the timescale of crustal cooling.

Another complication is the expected *external* heating of the stellar surface bombarded by magnetospheric particles. This heating occurs at the footprint of the current-carrying magnetic field lines (“j-bundle”). As the magnetosphere slowly untwists, the j-bundle shrinks and so does its hot footprint (Beloborodov 2009). Such shrinking hot spots have been observed in several transient magnetars, including the canonical transient mag-

netar XTE J1810-197. Following an outburst in 2003 it showed an X-ray afterglow decaying on a year timescale, with luminosity $\mathcal{L} \sim 2 \times 10^{34}$ erg s $^{-1}$ at $t \sim 1$ yr (Gotthelf & Halpern 2007). The observed area $A(t)$ and luminosity $\mathcal{L}(t)$ of the hot spot evolved in agreement with the predictions of the untwisting magnetosphere model. Similar shrinking hot spots were observed in 1E 1547.0-5408, CXOU J164710.2-455216, SGR 0501+4516, SGR 0418+5729 (see the data collection in Beloborodov (2011) and references therein) and more recently in Swift J1822.3-1606 (Scholz et al. 2014) and the Galactic Center magnetar SGR J1745-2900 (Coti Zelati et al. 2015).

Strong Alfvén waves and deep plastic heating are certainly expected in energetic events, in particular in giant flares. All three giant flares observed to date were emitted by persistently active magnetars, which maintain a high level of both magnetospheric activity and surface luminosity. It is possible that plastic damping of Alfvén waves is the main mechanism that keeps the crust hot in these objects.

This work was supported by NASA grant NNX13AI34G.

REFERENCES

- An, H., Kaspi, V. M., Tomsick, J. A., et al. 2012, *ApJ*, 757, 68
 Beloborodov, A. M. 2009, *ApJ*, 703, 1044
 Beloborodov, A. M. 2011, in *High-Energy Emission from Pulsars and their Systems*, ed. D. F. Torres & N. Rea, 299
 —. 2013, *ApJ*, 762, 13
 Beloborodov, A. M., & Levin, Y. 2014, *ApJ*, 794, L24
 Beloborodov, A. M., & Thompson, C. 2007, *ApJ*, 657, 967
 Blaes, O., Blandford, R., Goldreich, P., & Madau, P. 1989, *ApJ*, 343, 839
 Brown, E. F., & Cumming, A. 2009, *ApJ*, 698, 1020
 Chugunov, A. I., & Horowitz, C. J. 2010, *MNRAS*, 407, L54
 Coti Zelati, F., Rea, N., Papitto, A., et al. 2015, *MNRAS*, 449, 2685
 Enoto, T., Nakagawa, Y. E., Sakamoto, T., & Makishima, K. 2012, *MNRAS*, 427, 2824
 Esposito, P., Israel, G. L., Zane, S., et al. 2008, *MNRAS*, 390, L34
 Fitzpatrick, R. 2013, *Oscillations and Waves: An Introduction* (CRC Press)
 Gotthelf, E. V., & Halpern, J. P. 2007, *Ap&SS*, 308, 79
 Haensel, P., & Potekhin, A. Y. 2004, *A&A*, 428, 191
 Irgens, F. 2008, *Continuum Mechanics* (Springer)
 Kaminker, A. D., Yakovlev, D. G., Potekhin, A. Y., et al. 2006, *MNRAS*, 371, 477
 Kuiper, L., Hermsen, W., den Hartog, P. R., & Urama, J. O. 2012, *ApJ*, 748, 133
 Lyubarsky, Y., Eichler, D., & Thompson, C. 2002, *ApJ*, 580, L69
 Lyutikov, M. 2015, *MNRAS*, 447, 1407
 Mereghetti, S. 2008, *A&A Rev.*, 15, 225
 Mereghetti, S., Esposito, P., Tiengo, A., et al. 2006, *A&A*, 450, 759
 Piro, A. L. 2005, *ApJ*, 634, L153
 Pons, J. A., Miralles, J. A., & Geppert, U. 2009, *A&A*, 496, 207
 Potekhin, A. Y. 1999, *A&A*, 351, 787
 Potekhin, A. Y., & Yakovlev, D. G. 2001, *A&A*, 374, 213
 Potekhin, A. Y., Yakovlev, D. G., Chabrier, G., & Gnedin, O. Y. 2003, *ApJ*, 594, 404
 Rea, N., Israel, G. L., Esposito, P., et al. 2012, *ApJ*, 754, 27
 Scholz, P., Kaspi, V. M., & Cumming, A. 2014, *ApJ*, 786, 62
 Scholz, P., Ng, C.-Y., Livingstone, M. A., et al. 2012, *ApJ*, 761, 66
 Sotani, H., Kokkotas, K. D., & Stergioulas, N. 2007, *MNRAS*, 375, 261
 Thompson, C., & Blaes, O. 1998, *Phys. Rev. D*, 57, 3219
 Thompson, C., & Duncan, R. C. 1996, *ApJ*, 473, 322
 Thompson, C., Lyutikov, M., & Kulkarni, S. R. 2002, *ApJ*, 574, 332
 Thorne, K. S. 1977, *ApJ*, 212, 825
 Woods, P. M., Kouveliotou, C., Göğüş, E., et al. 2001, *ApJ*, 552, 748
 Woods, P. M., & Thompson, C. 2006, *Soft gamma repeaters and anomalous X-ray pulsars: magnetar candidates*, ed. W. H. G. Lewin & M. van der Klis, 547–586
 Yakovlev, D. G., & Pethick, C. J. 2004, *ARA&A*, 42, 169